



# Facile preparation of magnetic P(MMA-co-GMA)@Fe<sub>3</sub>O<sub>4</sub>@PMAA microspheres using porous microsphere as templates for removal of methylene blue

Jinquan Zhang<sup>1</sup> · Hong Man<sup>2</sup> · Xuelian Han<sup>3</sup> · Zhifei Wang<sup>1</sup> · Yong Jiang<sup>1</sup>

Received: 2 February 2023 / Revised: 17 March 2023 / Accepted: 23 March 2023 / Published online: 3 May 2023  
© The Author(s), under exclusive licence to Springer-Verlag GmbH Germany, part of Springer Nature 2023

## Abstract

Magnetic polymer microspheres (MPMs) have been frequently used in contemporary wastewater treatment technology because of their efficient adsorption and separation capabilities. However, the magnetization efficiency of polymer microspheres cannot be effectively enhanced using the reported template methods. In this study, a novel template method for preparing MPMs was developed. Magnetic P(MMA-co-GMA)@Fe<sub>3</sub>O<sub>4</sub>@PMAA microspheres (mPFPMs) were created with a high magnetic content, homogeneous particle size distribution, and carboxylated surfaces. Compared with the conventional template methods, this method avoids the generation of free magnetic nanoparticles and improves the magnetic content of MPMs, as well as imparting carboxyl functional groups to the mPFPMs. The mPFPMs can be used to adsorb contaminants quickly and effectively. The results of the adsorption process were preferably fitted to the Langmuir isotherm ( $R^2=0.998$ ) with a maximum adsorption capacity of 124.9 mg/g and followed the pseudo-second-order kinetic model. Besides, the mPFPMs adsorbent showed better reusability for ten cycles with high adsorption properties. Therefore, this work proposed a novel and facile strategy to prepare MPMs that exhibited significant potential application value in many fields.

**Keywords** Magnetic polymer microspheres · Template method · Porous microspheres · Adsorption of dyes

## Introduction

The removal of various contaminants (including dyes, heavy metal ions, and organic pollutants) from water is a prominent issue, as they can cause serious health problems [1, 2]. Several methods, including layer crystallization technology, photocatalytic treatment, electrocoagulation process, and electrostatic attraction-adsorption, have been used to achieve heavy metal ions and dyes removal [2–5]. Among them, the electrostatic attraction-adsorption method is a better choice because of its high efficiency and low cost [6]. In recent years, various adsorbents, such as carbonaceous composite

material, modified hydrogel, molecularly imprinted materials, chitosan-based composite, silicate materials and graphene oxide, have been applied for removing dyestuffs from aqueous water [7–12]. However, most adsorbents that have been reported have problems, such as complex processes, long times, and low recycling performance, which limit their practical application [13–16].

In recent years, magnetic polymer microspheres (MPMs) used as adsorbents in wastewater treatment have become a research hotspot [17]. MPMs possessed the benefits of magnetic nanoparticles and polymers. For one thing, magnetic nanoparticles enabled the adsorbent to be quickly separated in a magnetic field. For another thing, adsorption efficiency could be significantly improved with the use of polymers, because of the functional groups and high specific surface areas [18, 19]. The reported preparation methods of MPMs involved solvothermal method, monomer polymerization, template in situ generation, and template assembly [20–24]. Solvothermal method was capable of preparing MPMs with uniform particle size and strong magnetic properties, but it was difficult to scale up and was associated with high safety risks. For instance, Gao et al. reported the synthesis of silica

✉ Yong Jiang  
yj@seu.edu.cn

<sup>1</sup> School of Chemistry and Chemical Engineering, Southeast University, Nanjing 211189, People's Republic of China

<sup>2</sup> Luzhi Senior High School, Suzhou 215127, People's Republic of China

<sup>3</sup> Research and Development Department, Haichang Contact Lens Co, Ltd, Danyang 212331, People's Republic of China

coated  $\text{Fe}_3\text{O}_4$  magnetic colloidal nanocrystal clusters [25]. Monomer polymerization could be used to prepare MPMs with different surfaces. For example, Dou et al. created epoxy-functionalized magnetic polymer core–shell microspheres using glycidyl methacrylate as monomer. However, due to the weak interaction between the monomer and the magnetic nanoparticles, the prepared MPMs typically had small particle sizes (usually 100–200 nm), wide particle size distribution, and unequal magnetic content [26–29]. Furthermore, the above problems were difficult to solve simultaneously due to the nature of monomer polymerization [30, 31].

To solve these problems, the template method had been given more and more attention [32]. A typical step was that polymer microspheres were used as templates, magnetic nanoparticles were deposited on the templates, and finally they were encapsulated [33]. The presence of template polymer microspheres resulted in the homogeneous and tunable particle size of MPMs [34]. The surface coatings could be made functional by the encapsulating technique [35]. For example, Yu et al. [36] created  $\text{PMMA}@Fe_3O_4@DR$  MPMs by depositing  $\text{Fe}_3\text{O}_4$  nanoparticles onto porous polymethylmethacrylate microspheres, which acted as templates, then encasing those microspheres in photosensitive diazo resin to increase stability. Additionally, the performance of the MPMs was investigated for the removal of anions and aromatic dyes from wastewater. However, the reported template methods for producing MPMs required a long time in solution for the template polymer microspheres to adsorb and chelate metal ions [37–42]. Adsorption, deposition, and centrifugation operations must be repeated in a laborious and time-consuming manner in order to deposit as many magnetic nanoparticles as possible in the template polymer microspheres [43–48]. Further, a number of wrapping and coating techniques have been investigated to prevent the magnetic nanoparticles deposited on the templated polymer microspheres from falling off during use. However, most of them had disadvantages such as adhesion, uneven distribution of surface coatings, and complicated processes [49–51]. Consequently, it was still necessary to develop a novel and facile template method to prepare MPMs with a narrow particle size distribution, high magnetic content, and functionalized surfaces.

Therefore, in this article, we developed a novel and facile template method to prepare MPMs. Firstly, monodisperse carboxylated porous  $\text{P(MMA-co-GMA)}$  microspheres were used as templates. Then,  $\text{Fe}_3\text{O}_4$  nanoparticles were generated in situ inside and on the surfaces of the templates through a hydrothermal precipitation method. Finally, magnetic  $\text{P(MMA-co-GMA)}@Fe_3O_4@PMAA$  microspheres (mPFPMs) were obtained by reflux precipitation polymerization [52]. In this work, the magnetization of template polymer microspheres was accomplished via the hydrothermal precipitation process.  $\text{Fe}_3\text{O}_4$  nanoparticles were

securely adhered to the surface and interior of  $\text{P(MMA-co-GMA)}$  microspheres. The formation of free  $\text{Fe}_3\text{O}_4$  nanoparticles was avoided while increasing the magnetic content of mPFPMs. Furthermore, the surfaces of mPFPMs were endowed with carboxyl functional groups during polymeric encapsulation. The experimental procedure for the preparation of MPMs using the template method was simplified by these two features. The size of template polymer microspheres and the categories of monomers could be changed to prepare different types of MPMs. Under different adsorption control parameters, the ability of mPFPMs to absorb MB from wastewater was investigated. The adsorption process was analyzed isothermally and kinetically, and its reusability was assessed [53–55]. The mPFPMs had been proven to work as an effective, long-lasting, and sustainable adsorbent for water treatment.

## Experimental

### Materials

Styrene (St), isopropyl alcohol (IPA), glycidyl methacrylate (GMA), methyl methacrylate (MMA), divinylbenzene (DVB), sodium lauryl sulfate (SDS), benzoyl peroxide (BPO), toluene, and methylene blue (MB) were purchased from Shanghai Macklin Biochemical Technology Co., Ltd. Polyvinylpyrrolidone (PVP, MW = 40,000 g/mol) was commercially available from Yuanye Biotechnology Co., Ltd. (Shanghai, China). Azobisisobutyronitrile (AIBN) was obtained from Shanghai Titan Technology Co., Ltd. Dibutyl phthalate (DBP), acetonitrile, hexamethylene tetramine (HETM), and ethyleneglycol (EG) were provided by Shanghai Lingfeng Chemical Reagent Co., Ltd.  $\text{FeCl}_2 \cdot 4\text{H}_2\text{O}$ ,  $N,N'$ -methylenebisacrylamide (MBA), methacrylic acid (MAA), sodium hydroxide (NaOH), and hydrochloric acid were supplied by Sinopharm Chemical Reagent Co., Ltd. (Shanghai, China).

### Synthesis of porous template $\text{P(MMA-co-GMA)}$ microspheres

A simple dispersion polymerization method was used to prepare monodisperse Polystyrene (PS) microspheres [56]. Under magnetic stirring, all of the styrene (2.5 mL), PVP (0.45 g), and AIBN (0.05 g) were dissolved in 20 mL IPA and 15 mL water to form a homogeneous solution. Pure nitrogen gas was bubbled into the solution at room temperature for roughly 1 h to deoxygenate it. Then the reaction was heated to 75°C and kept for 12 h under constant stirring at a rate of 400 rpm. After the reaction, the resultant dispersion was centrifuged, multiple times rinsed with ethanol, and then dried for 24 h at room temperature in a vacuum oven.

A modified two-step seed swelling method was used to fabricate porous microspheres. 0.6 mL of toluene and 1.8 mL of DBP were added to a 0.15% SDS aqueous solution, and the mixture was thoroughly emulsified by ultrasonic. After that, 0.1 g of the previously manufactured PS seed microspheres were added, and they were swelled at 30 °C for 12 h. The addition of 2.65 mL of MMA, 0.55 mL of DVB, 0.46 mL of GMA, and 0.12 g of BPO to a 0.15% SDS aqueous solution resulted in a fully emulsified mixture. The reaction solution was combined with the emulsified solution above, which then swelled at 30 °C for 6 h. Ultimately, the temperature was raised to 70 °C, and the polymerization reaction was continued for 16 h in a nitrogen-protected environment. The reaction solution was centrifuged, washed with ethanol and water three times, and dried in a vacuum drying oven to create porous P(MMA-co-GMA) microspheres.

1.0 g of porous P(MMA-co-GMA) microspheres were dissolved in 50 mL of a 10% NaOH solution, hydrolyzed for 8 h at 60 °C, and neutralized with distilled water. The microspheres were then mixed at 80 °C for 4 h with a 50 mL solution of 0.2 mol/L H<sub>2</sub>SO<sub>4</sub>. The product was washed with water until neutral and dried in a vacuum drying oven for 16 h to obtain twice-hydrolyzed porous template P(MMA-co-GMA) microspheres.

### Preparation of magnetic P(MMA-co-GMA)@Fe<sub>3</sub>O<sub>4</sub> microspheres

A hydrothermal precipitation method was used to prepare magnetic P(MMA-co-GMA)@Fe<sub>3</sub>O<sub>4</sub> microspheres. Firstly, 0.16 g of twice-hydrolyzed porous template P(MMA-co-GMA) microspheres were dispersed in a solution consisting of 40 mL of water and 10 mL of EG. The mixture was treated by ultrasound for 20 min to obtain a white emulsion. Then, 0.08 g FeCl<sub>2</sub>•4H<sub>2</sub>O and 0.05 g HETM were added into the emulsion with a mechanical stirrer for 10 min to obtain a yellow flocculent solution, and then the reaction was carried out under a nitrogen atmosphere at a temperature of 80 °C for 1 h. Finally, after the reaction completed, the product was magnetically separated after the addition of water and then washed 5 times with 100 mL of water to obtain magnetic P(MMA-co-GMA)@Fe<sub>3</sub>O<sub>4</sub> microspheres.

### Preparation of magnetic P(MMA-co-GMA)@Fe<sub>3</sub>O<sub>4</sub>@PMAA microspheres

Reflux precipitation polymerization was used to synthesize mPFPMs. 0.04 g of magnetic P(MMA-co-GMA)@Fe<sub>3</sub>O<sub>4</sub> microspheres were dispersed in 45 mL of acetonitrile. After 0.4 g MAA, 0.1 g MBA, and 0.02 g AIBN were added

rapidly and continuously, the mixture was heated to 80 °C for 2 h. The mPFPMs were washed with distilled water at room temperature.

### Characterization

On the Nicolet-5700 spectrum (Asheville) and UV-2600 spectrum (Shimadzu, Japan), the FT-IR and UV-vis absorption spectra were conducted. Transmission electron microscopy (TEM; FEI, USA) and field-emission scanning electron microscopy (SEM; FEI Inspect F50, USA) were used to describe the morphologies of the materials. Energy-dispersive X-ray spectroscopy (EDX), in conjunction with TEM and SEM, was used to obtain the mapping of the element distribution. The crystalline structure patterns of the magnetic microspheres were discovered using Ultima IV powder X-ray diffraction (XRD; Shimadzu, Japan). The TG-209 F-3 equipment (NETZSCH, Germany) was used for the thermogravimetric analysis (TGA). The microspheres were heated in oxygen at a scan rate of 20 °C/min to 750 °C. The magnetism of these microspheres was studied using the VSM-7407 vibrating sample magnetometer (VSM, Lake Shore). The N<sub>2</sub> adsorption-desorption experiment was carried out using an ASAP-2460 Brunner-Emmett-Teller analyzer (BET, Micromeritics) to determine the pore size distribution of the porous template P(MMA-co-GMA) microspheres. Mercury intrusion porosimetry (MIP) was carried out with the Porosizer 9520 equipment from Micromeritics Instrument Corporation, to determine the pore size distribution of mesopores and macropores in the microsphere fraction. The particle size and zeta potential of the samples were tested and analyzed by the NanoBrook multi-angle particle size potential analyzer from Brookhaven, USA.

### MB sorption experiments

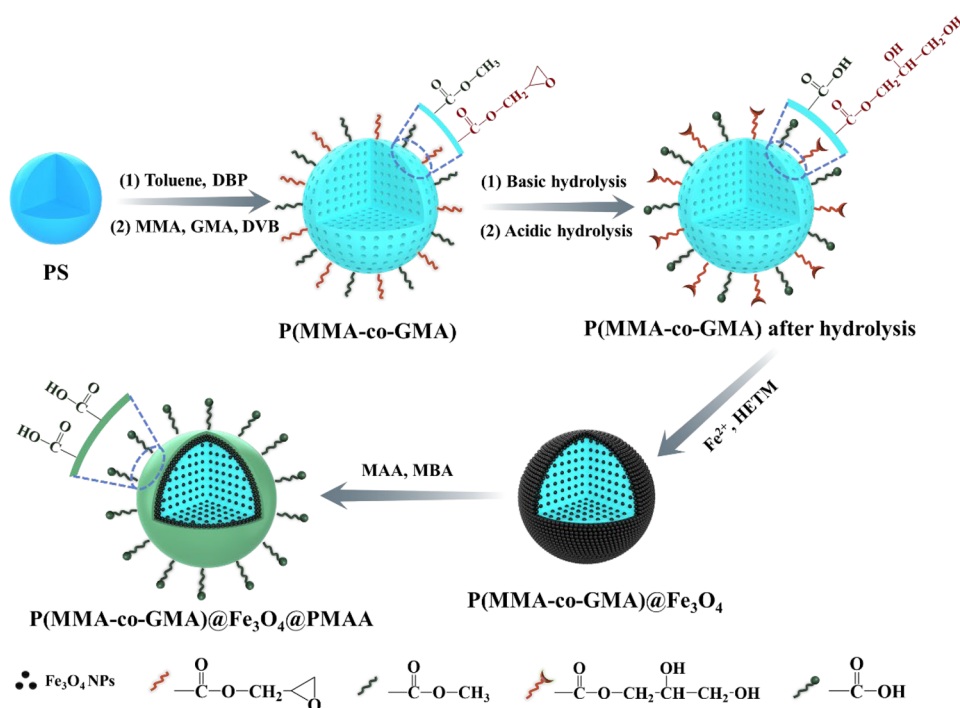
In batch adsorption tests, the adsorption process was evaluated by introducing 6 mg of mPFPMs adsorbent to 30 mL of MB dye solution (2–40 mg/L). The pH was adjusted using 0.1 M of both HCl and NaOH in a range of 1 to 12. The trials were performed between 298 and 328 K. The following formulas were used to calculate the removal efficiency (R%) and adsorption capacity (Q<sub>e</sub>, mg/g) and (Q<sub>t</sub>, mg/g).

$$R(\%) = \frac{C_0 - C_e}{C_0} \times 100\% \quad (1)$$

$$Q_e(\text{mg/g}) = (C_0 - C_e) \times \frac{V}{m} \quad (2)$$

$$Q_t(\text{mg/g}) = (C_0 - C_t) \times \frac{V}{m} \quad (3)$$

**Scheme 1** Schematic illustration of the synthesis procedure of magnetic P(MMA-co-GMA)@Fe<sub>3</sub>O<sub>4</sub>@PMAA microspheres



where  $C_0$  (mg/L) was the initial MB concentration,  $C_e$  (mg/L) was the MB equilibrium concentration,  $C_t$  (mg/L) was the MB concentration at a given time  $t$ ,  $V$  was the volume (mL) of MB dye solution, and  $m$  (g) was the amount of mPFPMs.

A continuous adsorption–desorption cycle utilizing ethanol as the desorption solvent was performed in order to examine the repeated adsorption performance of mPFPMs on MB dyes. The mPFPMs were taken out of the adsorption medium when the adsorption process was finished, and they were soaked and agitated in ethanol for 1 h at room temperature. The mPFPMs were then vacuum-dried at room temperature after being washed with water.

## Result and discussion

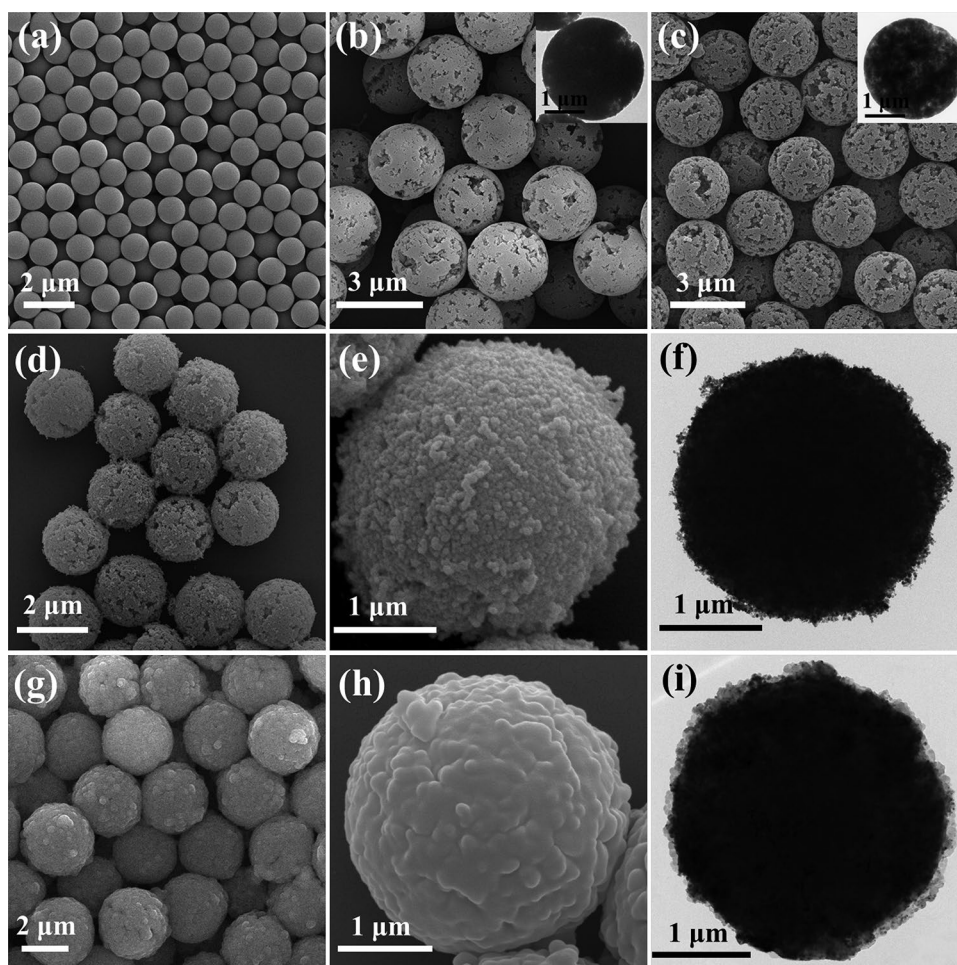
The steps required for the preparation of mPFPMs were outlined in Scheme 1. Firstly, dispersion polymerization was used to prepare monodisperse PS seed microspheres. A modified two-step swelling polymerization process was then used to synthesize porous P(MMA-co-GMA) microspheres. Following that, the ester and epoxy groups of porous P(MMA-co-GMA) microspheres were converted to carboxyl or hydroxyl groups under the action of base and acid hydrolysis. After that, the hydrolyzed porous P(MMA-co-GMA) microspheres were used as templates. Fe<sub>3</sub>O<sub>4</sub> nanoparticles were generated in situ inside and on the surfaces of the template polymer microspheres through a modified hydrothermal precipitation method. Finally, the

P(MMA-co-GMA)@Fe<sub>3</sub>O<sub>4</sub> microspheres were encapsulated and carboxylated through distillation precipitation polymerization to obtain mPFPMs. Compared with the traditional template methods, the synthesis process was simplified, and the magnetic content of MPMs was increased.

## Characterization of sample

In order to track the synthesis process, we used TEM and SEM to characterize the products of each step. As observed in Fig. 1(a), the PS seed microspheres prepared by dispersion polymerization were uniform on a large scale, with an average diameter of 1  $\mu\text{m}$ . Furthermore, the surfaces of the PS microspheres were clearly smooth. Compared with the PS microspheres, the porous P(MMA-co-GMA) microspheres maintained monodispersity but changed dramatically in both the average size and surface morphology (Fig. 1(b) and inset). The average size of the microspheres increased from 1  $\mu\text{m}$  to 2.6  $\mu\text{m}$  under the swelling effect of the porogenic agent, and the surfaces also showed a distinct porous structure. It was observed by TEM images that the porous structure was present not only on the surfaces but also in the interior of the microspheres. The average particle size of porous P(MMA-co-GMA) microspheres did not change significantly after hydrolysis by alkali and acid (Fig. 1(c) and inset), but the pores on the surface and inside of the microspheres increased significantly. This might be due to the etching effect of acid–base on the residual linear oligomers in the porous P(MMA-co-GMA) microspheres. These enriched porous structures would provide more binding sites

**Fig. 1** The morphology characterization of different microspheres. **a** SEM images of PS seed microspheres; **b** SEM and TEM (inset) images of porous P(MMA-co-GMA) microspheres; **c** SEM and TEM (inset) images of porous P(MMA-co-GMA) microspheres after acid–base hydrolysis; **d, e** SEM images of magnetic P(MMA-co-GMA)@Fe<sub>3</sub>O<sub>4</sub> microspheres with different magnifications; **f** TEM images of magnetic P(MMA-co-GMA)@Fe<sub>3</sub>O<sub>4</sub> microspheres; **g, h** SEM images of magnetic P(MMA-co-GMA)@Fe<sub>3</sub>O<sub>4</sub>@PMAA microspheres with different magnifications; **i** TEM images of magnetic P(MMA-co-GMA)@Fe<sub>3</sub>O<sub>4</sub>@PMAA microspheres



for subsequent in situ deposition of Fe<sub>3</sub>O<sub>4</sub> nanoparticles. The hydrolyzed porous P(MMA-co-GMA) microspheres were used as templates, and a modified hydrothermal precipitation method was used in order to make the magnetization process easier and more effective. Under the action of the abundant carboxyl groups and the pore structure of the template microspheres, ferrous ions were captured by coordination and electrostatic adsorption, and Fe<sub>3</sub>O<sub>4</sub> nanoparticles were generated in situ.

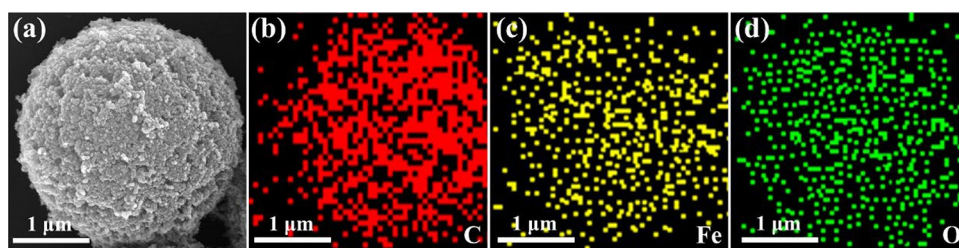
The morphology of P(MMA-co-GMA)@Fe<sub>3</sub>O<sub>4</sub> microspheres was observed by SEM (Fig. 1(d) and (e)) and TEM (Fig. 1(f)). Fe<sub>3</sub>O<sub>4</sub> nanoparticles were successfully filled into the template microsphere pores and formed a thin shell layer on the surface of the template microsphere. The average particle size of P(MMA-co-GMA)@Fe<sub>3</sub>O<sub>4</sub> microspheres was measured to be 2.7 μm. In addition, free Fe<sub>3</sub>O<sub>4</sub> nanoparticles were not found in a wide range, indicating that the Fe<sub>3</sub>O<sub>4</sub> nanoparticles were firmly attached to the template microspheres. As shown in Fig. 1(g) (h), P(MMA-co-GMA)@Fe<sub>3</sub>O<sub>4</sub>@PMAA microspheres had good monodispersity and smooth surfaces. The coating thickness was about 100 nm, as shown in Fig. 1(i), which provided good protection and

stability for the product microspheres. This demonstrated that the polymer encapsulation of magnetic P(MMA-co-GMA)@Fe<sub>3</sub>O<sub>4</sub> microspheres via distillation precipitation polymerization was effective.

Next, to confirm the distribution of Fe<sub>3</sub>O<sub>4</sub> nanoparticles on the surfaces of porous template P(MMA-co-GMA) microspheres, the magnetic P(MMA-co-GMA)@Fe<sub>3</sub>O<sub>4</sub> microspheres were characterized by EDX mapping. As shown in Fig. 2, Fe<sub>3</sub>O<sub>4</sub> nanoparticles were distributed over the whole template microsphere surface, and the distribution of Fe<sub>3</sub>O<sub>4</sub> nanoparticles was essentially the same as that of carbon and oxygen. Therefore, the improved hydrothermal precipitation method was an efficient way to achieve the magnetization of carboxylated porous polymer microspheres.

Meanwhile, Fig. S1(a) and (b) exhibited the SEM images of magnetic P(MMA-co-GMA)@Fe<sub>3</sub>O<sub>4</sub> microspheres at different magnifications after being calcined at 600 °C for 24 h. The organic matter inside the composite microspheres was completely cleaved due to the high temperature. However, after losing the assistance of the template polymer microspheres, the remaining magnetic nanoparticles stay formed

**Fig. 2** **a** SEM images of magnetic P(MMA-co-GMA)@Fe<sub>3</sub>O<sub>4</sub> microspheres; **b–d** EDX mapping of magnetic P(MMA-co-GMA)@Fe<sub>3</sub>O<sub>4</sub> microspheres



into spheres. This indicated that a large number of magnetic nanoparticles were successfully deposited on the surface of the template polymer microspheres.

To further determine the distribution of Fe<sub>3</sub>O<sub>4</sub> nanoparticles inside the P(MMA-co-GMA)@Fe<sub>3</sub>O<sub>4</sub>@PMAA microspheres, the ultrathin sections of P(MMA-co-GMA)@Fe<sub>3</sub>O<sub>4</sub>@PMAA microspheres were characterized by TEM. As shown in Fig. 3, it could be visualized that Fe<sub>3</sub>O<sub>4</sub> nanoparticles were uniformly dispersed inside the P(MMA-co-GMA)@Fe<sub>3</sub>O<sub>4</sub>@PMAA microspheres. This indicated that Fe<sub>3</sub>O<sub>4</sub> nanoparticles were successfully attached to the internal pores of template P(MMA-co-GMA) microspheres, and they were stabilized due to polymerization encapsulation.

Figure 4(a) showed the FT-IR spectra of PS seed microspheres, P(MMA-co-GMA) microspheres, P(MMA-co-GMA) microspheres after acid–base hydrolysis, P(MMA-co-GMA)@Fe<sub>3</sub>O<sub>4</sub> microspheres, and P(MMA-co-GMA)@Fe<sub>3</sub>O<sub>4</sub>@PMAA microspheres. The line a showed the typical absorption peaks of PS microspheres, including 3024, 1492, 1452, and 698 cm<sup>-1</sup>. The line b represented P(MMA-co-GMA) microspheres, and the absorption peaks at 1730 cm<sup>-1</sup> and 910 cm<sup>-1</sup> could be observed, which was attributed to the C=O stretching vibration of the ester group and the stretching vibration of the epoxy group. It indicated that GMA

and MMA monomers were successfully bound to the seed microspheres by solvation polymerization. The IR spectra of P(MMA-co-GMA) microspheres treated with alkali acid hydrolysis were shown in line c. The C=O stretching vibration peak of the carboxyl group at 1730 cm<sup>-1</sup> and the -OH stretching vibration peak at 3500 cm<sup>-1</sup> were significantly enhanced, while the characteristic peak of the epoxy group at 910 cm<sup>-1</sup> almost disappeared. This implied that the ester group was converted to the carboxyl group under alkaline hydrolysis, while the epoxy group was opened by acidic hydrolysis to release the hydroxyl group. Porous template polymer microspheres with rich carboxyl and hydroxyl groups were successfully prepared. Ferrous ions would be chelated and adsorbed by these functional groups in the next step of the magnetization reaction, so that Fe<sub>3</sub>O<sub>4</sub> nanoparticles were generated only on the surface and in the internal pores of the template microspheres. In the line d, the Fe–O stretching vibration absorption peak at 590 cm<sup>-1</sup> confirmed the formation of Fe<sub>3</sub>O<sub>4</sub>. Meanwhile, the C=O stretching vibration peak and the -OH stretching vibration peak were significantly weakened, which indicated that the carboxyl and hydroxyl groups were consumed due to the auxiliary Fe<sub>3</sub>O<sub>4</sub> generation. As shown in the line e, 1664 cm<sup>-1</sup> and 1525 cm<sup>-1</sup> indicated the carbonyl units and N–H units of the amide group in the MBA monomer, respectively. The strong absorption peak at 1730 cm<sup>-1</sup> was attributed to the stretching vibration of the carboxyl carbonyl unit in the MAA component, and the absorption peak at 590 cm<sup>-1</sup> was weakened because of polymerization encapsulation. These results confirmed the successful encapsulation of the copolymer shell layer of MAA and MBA on P(MMA-co-GMA)@Fe<sub>3</sub>O<sub>4</sub> microspheres. In addition, the abundant carboxyl functional groups on the surface of the polymer shell layer provided the practical performance of the product microspheres. In summary, P(MMA-co-GMA)@Fe<sub>3</sub>O<sub>4</sub> microspheres and P(MMA-co-GMA)@Fe<sub>3</sub>O<sub>4</sub>@PMAA microspheres have been successfully synthesized.

Figure 4(b) presented the XRD spectrum of P(MMA-co-GMA) microspheres after hydrolysis, P(MMA-co-GMA)@Fe<sub>3</sub>O<sub>4</sub> microspheres, and P(MMA-co-GMA)@Fe<sub>3</sub>O<sub>4</sub>@PMAA microspheres. The purple line was the XRD spectrum of P(MMA-co-GMA) microspheres after hydrolysis, which was clearly seen to have a broad diffraction peak only at about 20°, which was usually a characteristic peak for

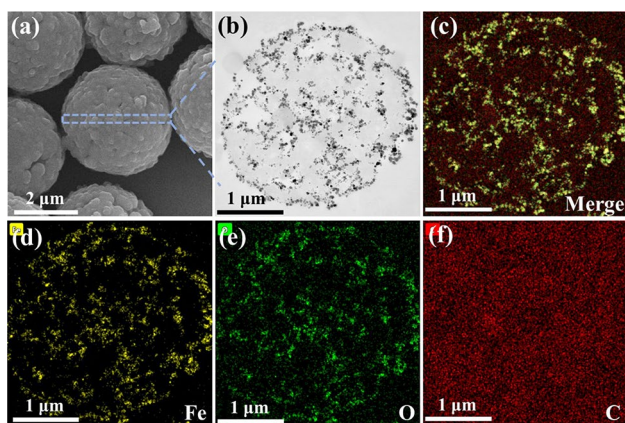


**Fig. 3** **a** SEM images of magnetic P(MMA-co-GMA)@Fe<sub>3</sub>O<sub>4</sub>@PMAA microspheres; **(b)** TEM images of ultrathin sections of magnetic P(MMA-co-GMA)@Fe<sub>3</sub>O<sub>4</sub>@PMAA microspheres; **(c–f)** EDX mapping for the ultrathin sections of magnetic P(MMA-co-GMA)@Fe<sub>3</sub>O<sub>4</sub>@PMAA microspheres

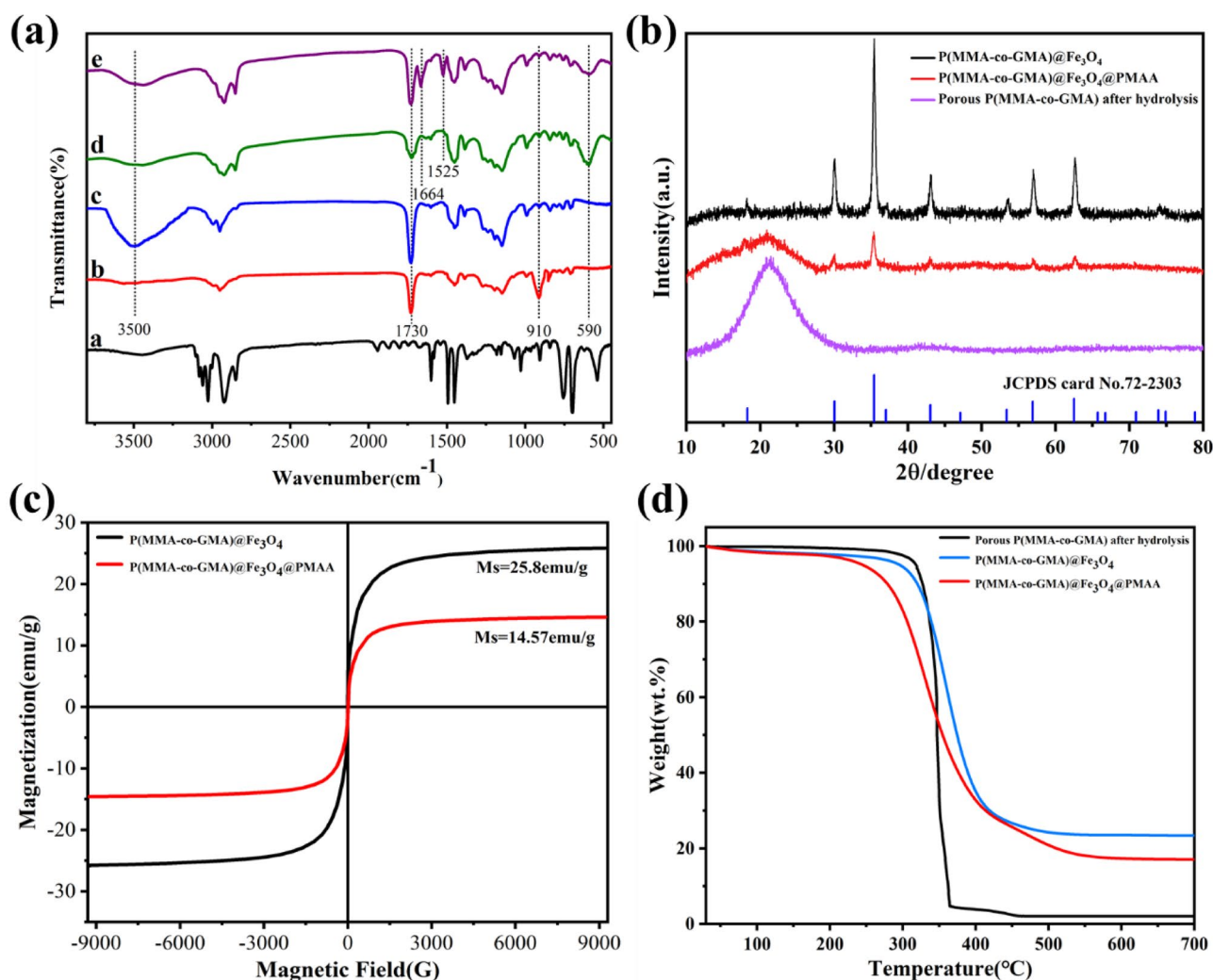


**Fig. 4** **a** FT-IR spectra of **a**) PS seed microspheres, **b**) P(MMA-co-GMA) microspheres, **c**) P(MMA-co-GMA) microspheres after acid–base hydrolysis, **d**) P(MMA-co-GMA)@Fe<sub>3</sub>O<sub>4</sub> microspheres, **e**) P(MMA-co-GMA)@Fe<sub>3</sub>O<sub>4</sub>@PMAA microspheres; **b**) XRD patterns of P(MMA-co-GMA) microspheres after acid–base hydrolysis, P(MMA-co-GMA)@Fe<sub>3</sub>O<sub>4</sub> microspheres, and P(MMA-co-GMA)@

Fe<sub>3</sub>O<sub>4</sub>@PMAA microspheres; **c**) Magnetization curves of P(MMA-co-GMA)@Fe<sub>3</sub>O<sub>4</sub> microspheres and P(MMA-co-GMA)@Fe<sub>3</sub>O<sub>4</sub>@PMAA microspheres; **d**) TGA curves of porous P(MMA-co-GMA) microspheres after hydrolysis, magnetic P(MMA-co-GMA)@Fe<sub>3</sub>O<sub>4</sub> microspheres, and magnetic P(MMA-co-GMA)@Fe<sub>3</sub>O<sub>4</sub>@PMAA microspheres

amorphous polymeric materials. The hydrolyzed P(MMA-co-GMA) microspheres were used as templates for the magnetization reaction with the help of their rich porous structure and functional groups. The black line was the XRD spectrum of P(MMA-co-GMA)@Fe<sub>3</sub>O<sub>4</sub> microspheres, the characteristic diffraction peaks at  $2\theta = 30.2^\circ$ ,  $35.4^\circ$ ,  $43.0^\circ$ ,  $53.3^\circ$ ,  $56.9^\circ$ , and  $62.5^\circ$  were attributed to the (220), (311), (400), (422), (333) and (440) lattice planes of cubic phase of Fe<sub>3</sub>O<sub>4</sub> (JCPDS standard card No. 72–2303). Meanwhile, the disappearance of the characteristic peaks of the amorphous polymer material implied that the Fe<sub>3</sub>O<sub>4</sub> nanoparticles form a shell layer, which completely encapsulated the template polymer microspheres. This was consistent with the SEM test results. In addition, no other signals were detected,

indicating that the preparation of magnetic P(MMA-co-GMA)@Fe<sub>3</sub>O<sub>4</sub> microspheres was successful. The XRD spectrum of P(MMA-co-GMA)@Fe<sub>3</sub>O<sub>4</sub>@PMAA was shown as the red line, where the characteristic peaks of the amorphous polymer material appeared once again and the characteristic diffraction peaks of Fe<sub>3</sub>O<sub>4</sub> were significantly weakened. This indicated that the copolymer coating was effective in encapsulating the P(MMA-co-GMA)@Fe<sub>3</sub>O<sub>4</sub> microspheres.

Figure 4(c) showed the magnetization curves of P(MMA-co-GMA)@Fe<sub>3</sub>O<sub>4</sub> microspheres and P(MMA-co-GMA)@Fe<sub>3</sub>O<sub>4</sub>@PMAA microspheres. It could be found that the saturation magnetization intensity value of P(MMA-co-GMA)@Fe<sub>3</sub>O<sub>4</sub> microspheres was 25.8 emu/g, and there

was no coercive force in magnetic field scanning. In contrast, the saturation magnetization intensity value of P(MMA-co-GMA)@Fe<sub>3</sub>O<sub>4</sub>@PMAA microspheres was 14.57 emu/g. This change could be observed more visually in Fig. S2(a) and (b). The magnetic separation time of P(MMA-co-GMA)@Fe<sub>3</sub>O<sub>4</sub> microspheres was 19 s, while that of P(MMA-co-GMA)@Fe<sub>3</sub>O<sub>4</sub>@PMAA microspheres was 33 s. There were two possible reasons for this phenomenon. On the one hand, the surface encapsulation of the polymer coating reduced the relative magnetic content of the microspheres, while on the other hand, the polymer coating was non-magnetic and had a shielding effect on the magnetic Fe<sub>3</sub>O<sub>4</sub> nanoparticles. When the external magnetic field was removed, the two magnetic microspheres mentioned above could be redistributed by a slight vibration. This feature enabled the economic and reusable applications of microspheres as adsorbents. It should be noted that the magnetic content of P(MMA-co-GMA)@Fe<sub>3</sub>O<sub>4</sub>@PMAA microspheres was enough to be easily separated from the solution in a magnetic field.

Figures 4(d) and S3 showed the TG/derivative thermogravimetry (DTG) plot of the products during the synthesis of magnetic P(MMA-co-GMA)@Fe<sub>3</sub>O<sub>4</sub>@PMAA microspheres. The weight loss process of the three samples could be roughly divided into three stages. The first stage was from the initial temperature to about 300 °C. This stage included the micro-weight loss process, mainly due to the evaporation of water physically adsorbed on the surfaces of the microspheres. The weight loss of the three samples was about 5% at this stage. The second stage was from 300 °C to about 400 °C. The weight loss from this process was much more significant. The weight loss rate of hydrolyzed porous P(MMA-co-GMA) microspheres was about 90%, which might attribute to the decomposition of polymer segments. In contrast, P(MMA-co-GMA)@Fe<sub>3</sub>O<sub>4</sub> microspheres and P(MMA-co-GMA)@Fe<sub>3</sub>O<sub>4</sub>@PMAA microspheres had a weight loss of about 65%, which was attributed to the decomposition of the uncrosslinked part of the microspheres. The final stage was 400–500 °C. The weight loss was slower, and the final curve tended to be flat. All organic matter had been decomposed, and the final undecomposed substance was Fe<sub>3</sub>O<sub>4</sub> nanoparticles. The mass fraction of Fe<sub>3</sub>O<sub>4</sub> nanoparticles in P(MMA-co-GMA)@Fe<sub>3</sub>O<sub>4</sub> microspheres and P(MMA-co-GMA)@Fe<sub>3</sub>O<sub>4</sub>@PMAA microspheres was calculated to be 26.4% and 18.4%, respectively.

In addition, the magnetic content of prepared mPFPMs and other MPMs reported in recent literature were shown in Table S1 for comparison. Obviously, the prepared mPFPMs had higher magnetic content value than several other MPMs, which had a great potential application in waste water treatment.

The pore size (including mesopores and macropores) distribution of porous P(MMA-co-GMA) microspheres before

and after hydrolysis treatment was tested by BET and MIP, and the results were shown in Fig. 5. Figure 5(a) and (c) showed that the adsorption isotherms were type IV and there were obvious hysteresis lines, indicating that the P(MMA-co-GMA) microspheres were typical porous materials. By Barrett-Joyner-Halenda (BJH) adsorption isotherm analysis, the average mesopore pore size of porous P(MMA-co-GMA) microspheres slightly decreased from 23.3 to 21.1 nm before and after hydrolysis treatment. This might be attributed to the weak etching effect of the high concentration of alkali-acid environment on P(MMA-co-GMA) microspheres, which produced more small pores below 20 nm. As shown in Fig. 5(b) and (d), the average macropore pore size of P(MMA-co-GMA) microspheres before and after the hydrolysis treatment was 624.4 nm and 668 nm, respectively. This indicated that the alkali-acid hydrolysis treatment not only carboxylated the microspheres, but also increased the pore size of the microspheres, which in turn increased the loading of magnetic Fe<sub>3</sub>O<sub>4</sub> nanoparticles.

### Methylene blue adsorption experiments

According to the characterization results, mPFPMs could be used as adsorbents for efficient adsorption of MB. The absorbance at 665 nm was measured by a UV Vis spectrophotometer. The concentration of MB could be determined from the standard curve (Fig. S4(a) and (b)).

### Effect of pH

The pH of the MB solution was critical to the adsorption capacity of adsorbents due to the charge distribution. Therefore, the effect of pH in the range of 1–12 on the adsorption capacity of mPFPMs was investigated. As shown in Fig. 6(a), the removal efficiency increased from 48.8 to 99.1% and the adsorption amount increased from 61 to 123.87 mg/g as the pH increased from 1 to 10. When the pH value exceeded 10, the removal efficiency and adsorption capacity showed a decreasing trend. To better explain the above phenomenon, the zeta potential of mPFPMs was examined at different pH values, and the results were shown in Fig. S4(c). The relatively high zeta potential at low pH (around –10 mV) indicated that the carboxyl groups on the surfaces of mPFPMs were protonated, forming a competitor for MB. As the pH of the solution increased, the zeta potential gradually decreased, indicating that a large amount of negative charge was generated on the surfaces of mPFPMs. The zeta potential was minimized at pH 10, which corresponded to the maximum adsorption obtained by mPFPMs at this time. As the pH continued to increase, no significant change in zeta potential was observed, indicating that the anionic carboxyl groups on the surfaces of mPFPMs had reached saturation.



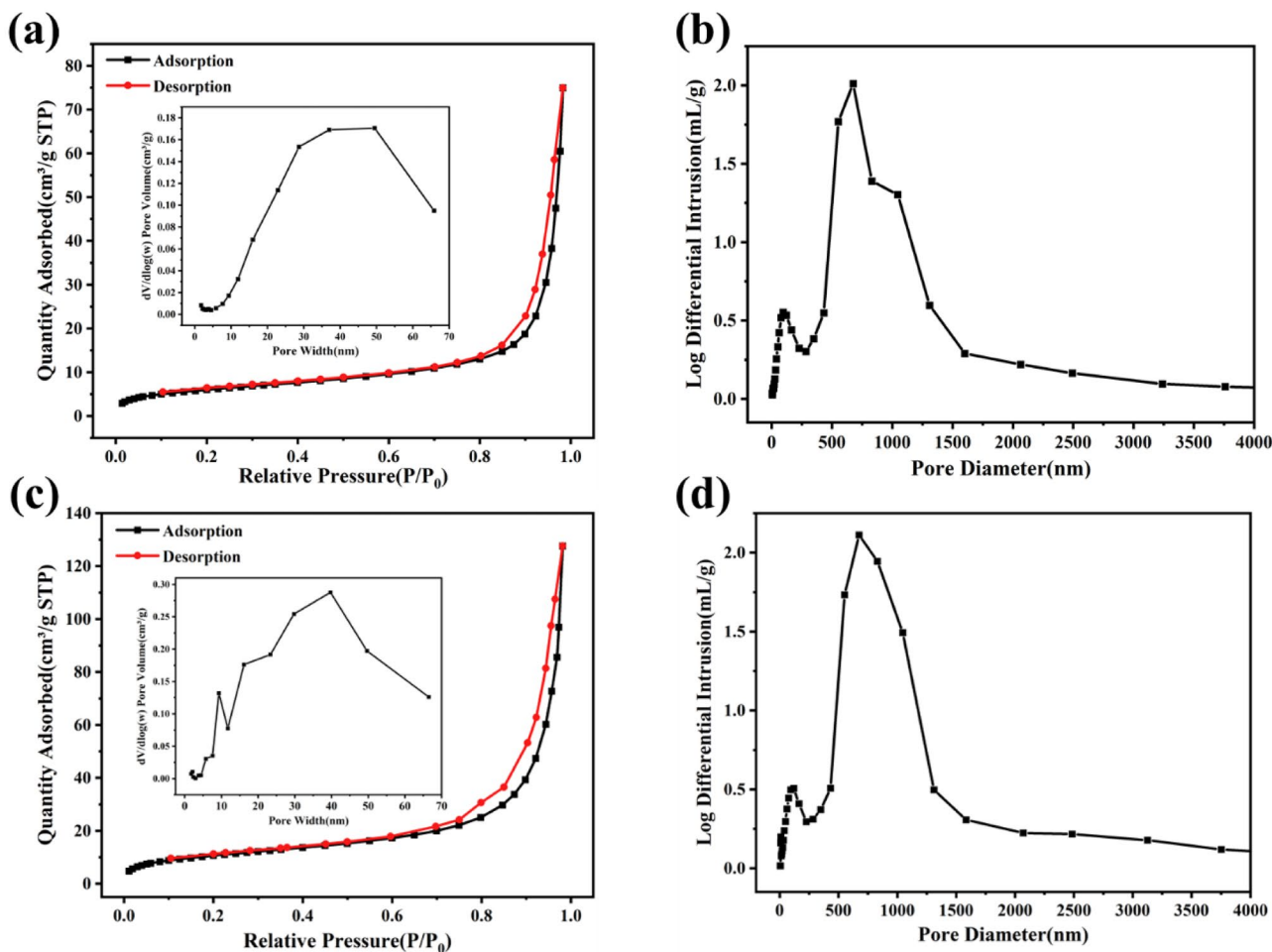


**Fig. 5** **a** Nitrogen sorption isotherm and the mesopore pore size distribution (inset) of porous P(MMA-co-GMA) microspheres; **b** Macropore pore size distribution of porous P(MMA-co-GMA) microspheres by MIP; **c** Nitrogen sorption isotherm and the mesopore pore

size distribution (inset) of porous P(MMA-co-GMA) microspheres after acid–base hydrolysis; **d** Macropore pore size distribution of porous P(MMA-co-GMA) microspheres after acid–base hydrolysis by MIP

### Effect of MAA content

The mass ratio of MAA and P(MMA-co-GMA)@Fe<sub>3</sub>O<sub>4</sub> microspheres was varied to investigate the effect of MAA content on the adsorption performance of mPFPMs, and the results were shown in Fig. 6(b). The mass ratio of MAA and P(MMA-co-GMA)@Fe<sub>3</sub>O<sub>4</sub> microspheres increased from 2:1 ( $R=21.8\%$ ,  $Q_e=27.25$  mg/g) to 10:1 ( $R=97.3\%$ ,  $Q_e=121.62$  mg/g). This suggested that with the increase in the number of carboxyl groups, MB was more readily adsorbed onto the mPFPMs by electrostatic interaction. However, when the MAA content continued to increase, the adsorption capacity did not change significantly, which was due to the saturation of all adsorptive sites on the mPFPMs surfaces with MB molecules.

### Effect of temperature

The effect of temperatures at 298, 308, 318 and 328 K on the adsorption of MB by mPFPMs was investigated. The results were shown in Fig. 6(c). When the temperature was increased from 298 to 328 K, the adsorption capacity decreased from 124.3 to 92.6 mg/g, indicating that the adsorption of MB by mPFPMs was an exothermic process and that the low temperature was more favorable to the adsorption process.

### Adsorbent reusability

Regeneration and reusability were crucial for the adsorbent material. To investigate the recyclability of mPFPMs, 10 adsorption–desorption cycles were performed under the

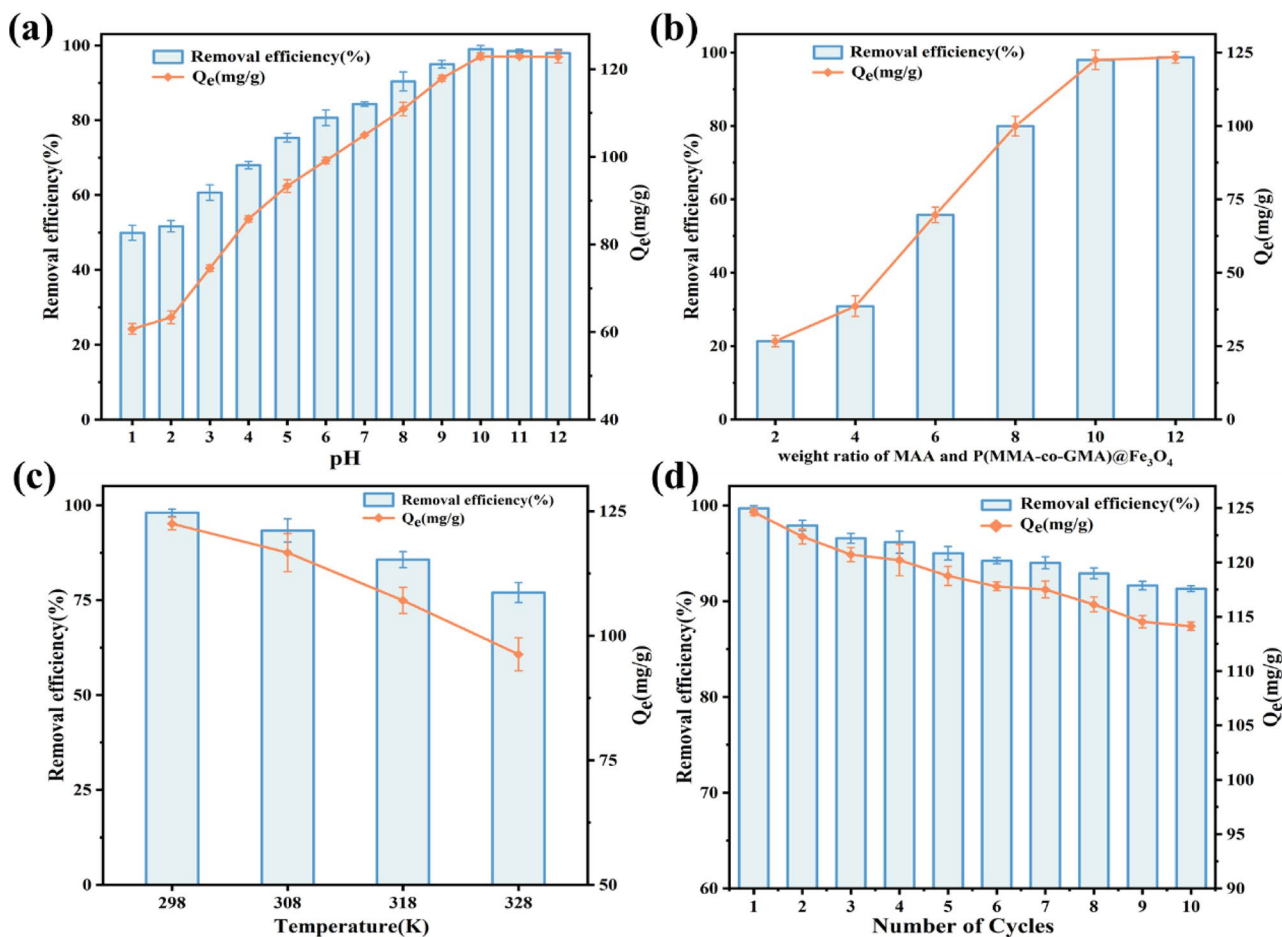


**Fig. 6** a Effect of pH for MB adsorption ( $T=298\text{ K}$ ,  $C_0=25\text{ mg/L}$ ); b effect of MAA content for MB adsorption ( $\text{pH}=10$ ,  $T=298\text{ K}$ ,  $C_0=25\text{ mg/L}$ ); c effect of temperature for MB adsorption ( $\text{pH}=10$ ,

$C_0=25\text{ mg/L}$ ); d reusability of mPFPMs for MB adsorption ( $\text{pH}=10$ ,  $T=298\text{ K}$ ,  $C_0=25\text{ mg/L}$ ). The error bars indicate the standard deviation from the mean ( $n=3$ )

same conditions, and the results were shown in Fig. 6(d). As could be seen from the figure, the adsorption capacity of the mPFPMs was gradually decreased with the increase of the number of cycles, but it was maintained at a high level. After ten consecutive adsorption–desorption cycles, the dye removal efficiency of the mPFPMs was still above 90%, and the maximum adsorption capacity reached 113.85 mg/g. This illustrated that the mPFPMs had good stability and recyclability.

**Adsorption isotherm**

The adsorption isotherms of mPFPMs on MB were investigated at 298 K and  $\text{pH}=10$ . As shown in Fig. 7(a), with the increase of MB equilibrium concentration, the adsorption capacity increased sharply at first, then gradually stabilized and reached the maximum value (124.97 mg/g).

The equilibrium adsorption data were fitted with the Langmuir isotherm model and the Freundlich isotherm

model, respectively, to better understand the adsorption mechanism. The Langmuir isotherm model assumed that the adsorption was a single molecular layer, where each molecule occupied only one adsorption site and there were no interactions between adsorbed molecules. In addition, the maximum adsorption capacity could be predicted by calculation. The Freundlich isotherm model was mainly used for multilayer adsorption, but could also be used for physical and chemical adsorption. The Langmuir isotherm equation could be described as:

$$\frac{C_e}{Q_e} = \frac{C_e}{Q_m} + \frac{1}{Q_m \cdot K_L} \tag{4}$$

The Freundlich isotherm equation could be described as:

$$\ln Q_e = \ln K_F + \frac{1}{n} \ln C_e \tag{5}$$

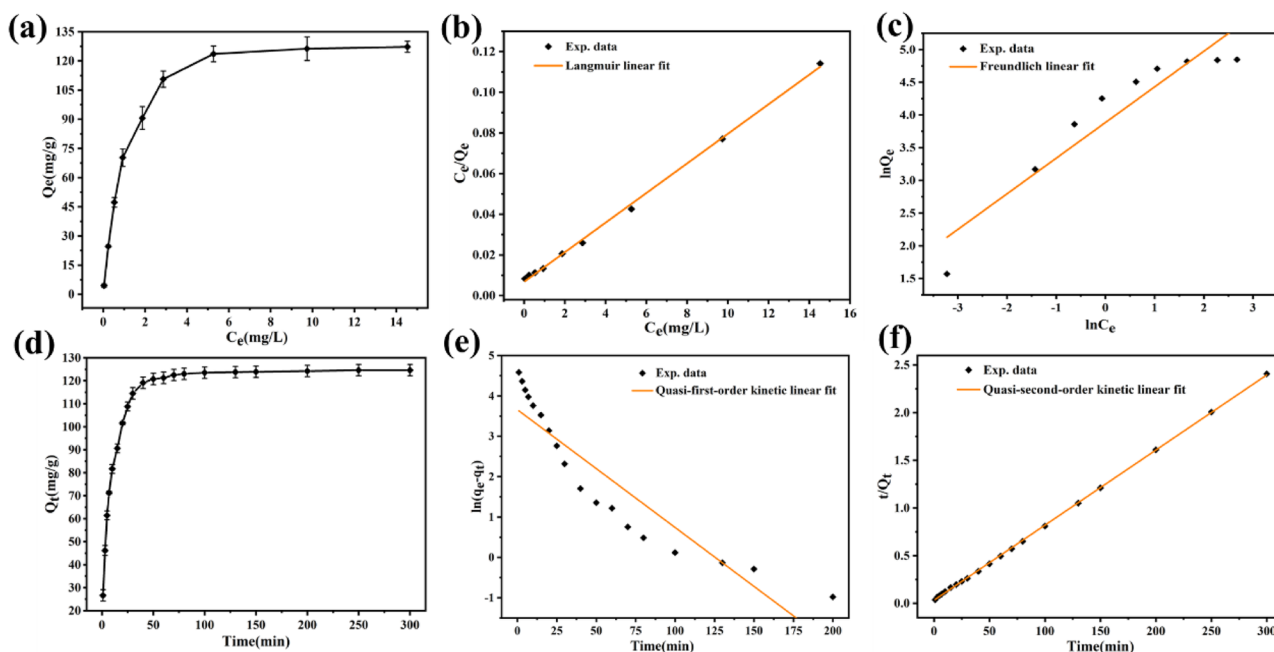


**Fig. 7** **a** Effect of initial MB concentration for MB adsorption; **b** Langmuir isotherms and **c** Freundlich isotherms for MB adsorption (pH=10, T=298 K). **d** Effect of adsorption time for MB adsorption;

**e** pseudo-first-order plots and **f** pseudo-second-order plots for MB adsorption (pH=10, T=298 K, C<sub>0</sub>=25 mg/L). The error bars indicate the standard deviation from the mean (n=3)

where the  $C_e$  (mg/L) was represented for the equilibrium adsorption concentration of MB; the  $Q_e$  (mg/g) was the equilibrium sorption capacity of adsorbent;  $Q_m$  (mg/g) was the theoretical maximum adsorption capacity of adsorbent;  $K_L$  (L/mg) was the Langmuir equilibrium constant;  $K_F$  (mg<sup>1-n</sup> L<sup>n</sup>/g) was the Freundlich equilibrium constant;  $1/n$  was the adsorption degree.

The results of the Langmuir and Freundlich adsorption isotherm fits were shown in Fig. 7(b) and (c), respectively. The relevant parameters were calculated according to Eqs. (4) and (5), and the results were shown in Table 1. The value of n obtained from the Freundlich model was greater than one, implying that the mPFPMs were favorable for the adsorption process of MB. It was clearly seen that the Langmuir model fits the adsorption isotherm ( $R^2=0.9978$ ) better than the Freundlich model ( $R^2=0.8731$ ), indicating that the adsorption process was monomolecular layer adsorption. The  $Q_m$  calculated from the Langmuir model was 126.33 mg/g, which was in good agreement with the experimental value (124.97 mg/g).

**Table 1** Sorption isotherm parameters for MB adsorption onto adsorbent (pH=10, 298 K)

Langmuir			Freundlich		
$Q_{max}$ (mg/g)	$K_L$ (L/mg)	$R^2$	$K_F$ (mg <sup>1-n</sup> ·L <sup>n</sup> /g)	n	$R^2$
126.333	1.2625	0.9978	48.638	1.822	0.87314

### Kinetic studies

The adsorption kinetics of mPFPMs on MB were investigated at pH=10 and room temperature. The effect of contact time on the adsorption capacity was shown in Fig. 7(d). It could be seen that the amount of MB adsorbed increased rapidly during the first 100 min of contact time, then increased slowly and finally remained at a certain level. Based on the above results, 150 min was chosen as the optimal time to ensure the equilibrium of the adsorption process.

The adsorption process was investigated using pseudo-first-order and pseudo-second-order kinetic models. The pseudo-first-order kinetic model assumed that the adsorption process was controlled by the diffusion process, and the pseudo-second-order kinetic model considered that the adsorption process was controlled by the chemisorption mechanism. The equations for each of the above two models were expressed as:

$$\ln(Q_e - Q_t) = \ln Q_e - k_1 \cdot t \tag{6}$$

$$\frac{t}{Q_t} = \frac{1}{k_2 \cdot Q_e^2} + \frac{t}{Q_e} \tag{7}$$

where  $Q_e$  (mg/g) was the adsorption capacity at equilibrium time,  $Q_t$  (mg/g) was the adsorption capacity at any time,  $k_1$  (min<sup>-1</sup>) and  $k_2$  (g/mg/min) were the pseudo-first-order rate constant and pseudo-second-order rate constant, respectively.

**Table 2** Fitting parameters of MB adsorption kinetic on prepared magnetic microspheres

Quasi-first-order kinetic model			Quasi-second-order kinetic model		
$k_1(\text{min}^{-1})$	$Q_e(\text{mg/g})$	$R^2$	$k_2(\text{g/mg}\cdot\text{min})$	$Q_e(\text{mg/g})$	$R^2$
0.02918	38.8322	0.8468	0.00194	126.9036	0.9998

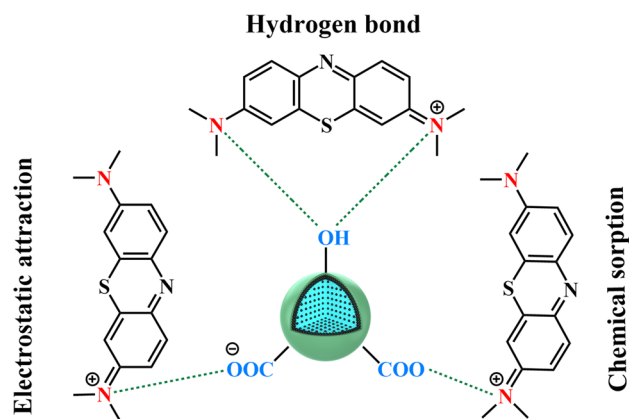
The fitted curves of the two kinetic models were shown in Fig. 7(e) and (f), respectively. The relevant parameters were calculated according to Eqs. (6) and (7), as shown in Table 2. According to the fitted curves and correlation coefficient ( $R^2$ ), the adsorption process of MB on mPFPMs belonged to the proposed second-order kinetic model. The adsorption process was controlled by the chemisorption mechanism, and the valence force generated by electron exchange between the adsorbent and the adsorbate was the rate-controlling step.

Above all, we could draw the conclusion that the adsorption process of MB was a Langmuir process and the adsorption behavior belonged to the pseudo-second-order model. The MB maximum adsorption capacity of prepared mPFPMs and other adsorbents reported in recent literature were shown in Table 3 for comparison. Obviously, the prepared mPFPMs were a more highly efficient adsorbent for the removal of MB than several other sorption materials, which had a great potential application in waste water treatment.

### Possible adsorption mechanism

Three main mechanisms of electrostatic attraction, hydrogen bonding interaction, and chemical sorption were proposed to explain the adsorption behaviors of MB on mPFPMs.

Electrostatic attraction is considered to be the main factor affecting the adsorption process. It relies on the relation between the pH of the zero-point charge ( $\text{pH}_{\text{zpc}}$ ) and the pH of solution [58–60]. When the pH value of the solution is higher than the  $\text{pH}_{\text{zpc}}$ , a strong electrostatic attraction will

**Fig. 8** The plausible mechanism for the removal of MB

occur between the adsorbent and the MB. On the contrary, with a pH value of the solution lower than  $\text{pH}_{\text{zpc}}$ , the electrostatic attraction will transfer into strong electrostatic repulsion. Moreover, MB is a cationic dye with a positive charge, and the surface of mPFPMs have a large amount of negatively charged carboxylate anion in the solution. The fast adsorption is mainly caused by strong electrostatic attraction between MB surface cations and mPFPMs surface anions. Therefore, it can draw the conclusion that the adsorption capacity is greatly affected by the pH value of solution and mainly relies on the electrostatic attraction between the adsorbent and MB.

Hydrogen bonding interaction also plays a role in the adsorption process. As is known to all, the hydrogen bond only exists between two atoms that have a relatively large electronegativity [57, 61]. With the formation of hydrogen bonds, the adsorption capacity of the adsorbent was enhanced. The prepared mPFPMs and MB can form the hydrogen bond between the H atom and N atom, thereby improving the adsorption capacity of the adsorbent.

Besides, according to the sorption kinetics, the sorption of MB on the mPFPMs conforms to the pseudo-second-order model, indicating that the adsorption behavior was

**Table 3** Comparison of MB maximum sorption capacity of prepared mPFPMs with other adsorbents

Adsorbents	$Q_{\text{max}}$ (mg/g)	References
Red mud@sucrose based carbon composite	76.92	[7]
Montmorillonite-reduced graphene oxide aerogel	450.90	[10]
sodium alginate/graphene oxide cellulose scaffold	51.55	[11]
$\text{Fe}_3\text{O}_4$ @lignosulfonate/phenolic microsphere	283.6	[55]
$\text{Fe}_3\text{O}_4$ @ $\text{SiO}_2$ -CR	31.44	[28]
Graphene Oxide	19.39	[57]
$\text{Fe}_3\text{O}_4$ @ $\text{SiO}_2$ -EDA-COOH	43.15	[53]
multi-carboxyl functionalized $\text{Fe}_3\text{O}_4$ @ $\text{SiO}_2$	37.52	[58]
Multifunctional PMMA@ $\text{Fe}_3\text{O}_4$ @DR	113.25	[36]
P(MMA-co-GMA)@ $\text{Fe}_3\text{O}_4$ @PMAA microspheres	124.97	This work

controlled by chemical sorption. The carboxyl anion in the adsorbent and the nitrogen atom in MB undergo electron transfer, forming an adsorption chemical bond [53]. Therefore, the adsorption capacity of MB has been enhanced. The possible adsorption mechanism of MB on the mPFPMs was schematically illustrated in Fig. 8.

## Conclusion

In conclusion, this work presented a novel and facile template method for preparing mPFPMs, and verified the feasibility of removing MB from aqueous solutions. Carboxylated P(MMA-co-GMA) porous microspheres were used as templates, which were first magnetized by a modified hydrothermal precipitation method and then encapsulated through reflux precipitation. Compared with the traditional template methods, this method avoided the tedious operation and generation of free magnetic nanoparticles during magnetization. In addition, the carboxyl functional modification was performed while encapsulating, which not only solved the problem of leakage of magnetic nanoparticles during use, but also avoided additional functional modification steps. The mPFPMs exhibited excellent absorption properties on MB dyes. The adsorption kinetics obeyed the pseudo-secondary model. The isothermal adsorption equilibrium data was in accordance with the Langmuir model. The maximum adsorption capacity of the single molecular layer was 124.97 mg/g. More importantly, the removal efficiency of the mPFPMs was still above 90% after 10 cycles, confirming that the mPFPMs were efficient and economical.

**Supplementary Information** The online version contains supplementary material available at <https://doi.org/10.1007/s00396-023-05099-w>.

**Funding** This work was supported by the Project Funded by the Priority Academic Program Development of Jiangsu Higher Education Institutions (PAPD) and the Fundamental Research Funds for the Central Universities with grant number 2242016K41020.

## Declarations

**Competing interests** The authors declare no competing interests.

## References

- Zhao X, Wang X, Lou T (2021) Preparation of fibrous chitosan/sodium alginate composite foams for the adsorption of cationic and anionic dyes. *J Hazard Mater* 403:124054. <https://doi.org/10.1016/j.jhazmat.2020.124054>
- Mohammed N et al (2021) Selective adsorption and separation of organic dyes using functionalized cellulose nanocrystals. *Chem Eng J* 417:129237. <https://doi.org/10.1016/j.cej.2021.129237>
- Liu C et al (2020) Fabrication and investigation on Ag nanowires/TiO<sub>2</sub> nanosheets/graphene hybrid nanocomposite and its water treatment performance. *Adv Compos Hybrid Mater* 3(3):402–414. <https://doi.org/10.1007/s42114-020-00164-2>
- Qi K et al (2020) Transition metal doped ZnO nanoparticles with enhanced photocatalytic and antibacterial performances: experimental and DFT studies. *Ceram Int* 46(2):1494–1502. <https://doi.org/10.1016/j.ceramint.2019.09.116>
- Nippatla N, Philip L (2019) Electrocoagulation-floatation assisted pulsed power plasma technology for the complete mineralization of potentially toxic dyes and real textile wastewater. *Process Saf Environ Prot* 125:143–156. <https://doi.org/10.1016/j.psep.2019.03.012>
- Liu Q et al (2020) Superior adsorption capacity of functionalised straw adsorbent for dyes and heavy-metal ions. *J Hazard Mater* 382:121040. <https://doi.org/10.1016/j.jhazmat.2019.121040>
- Kazak O, Eker YR, Akin I, Bingol H, Tor A (2017) A novel red mud@sucrose based carbon composite: preparation, characterization and its adsorption performance toward methylene blue in aqueous solution. *J Environ Chem Eng* 5(3):2639–2647. <https://doi.org/10.1016/j.jece.2017.05.018>
- Wang W, Tian G, Zhang Z, Wang A (2015) A simple hydrothermal approach to modify palygorskite for high-efficient adsorption of Methylene blue and Cu(II) ions. *Chem Eng J* 265:228–238. <https://doi.org/10.1016/j.cej.2014.11.135>
- Wan X, Rong Z, Zhu K, Wu Y (2022) Chitosan-based dual network composite hydrogel for efficient adsorption of methylene blue dye. *Int J Biol Macromol* 222:725–735. <https://doi.org/10.1016/j.ijbiomac.2022.09.213>
- Zhou S et al (2022) Montmorillonite-reduced graphene oxide composite aerogel (M-rGO): a green adsorbent for the dynamic removal of cadmium and methylene blue from wastewater. *Sep Purif Technol* 296:121416. <https://doi.org/10.1016/j.seppur.2022.121416>
- Al-Shemy MT, Al-Sayed A, Dacrory S (2022) Fabrication of sodium alginate/graphene oxide/nanocrystalline cellulose scaffold for methylene blue adsorption: kinetics and thermodynamics study. *Sep Purif Technol* 290:120825. <https://doi.org/10.1016/j.seppur.2022.120825>
- Gao T, Guan G, Wang X, Lou T (2022) Electrospun molecularly imprinted sodium alginate/polyethylene oxide nanofibrous membranes for selective adsorption of methylene blue. *Int J Biol Macromol* 207(March):62–71. <https://doi.org/10.1016/j.ijbiomac.2022.02.193>
- Jawad AH, Abdulhameed AS (2020) Mesoporous Iraqi red kaolin clay as an efficient adsorbent for methylene blue dye: adsorption kinetic, isotherm and mechanism study. *Surf Interfaces* 18:100422. <https://doi.org/10.1016/j.surf.2019.100422>
- Bello K, Sarojini BK, Narayana B, Rao A, Byrappa K (2018) A study on adsorption behavior of newly synthesized banana pseudo-stem derived superabsorbent hydrogels for cationic and anionic dye removal from effluents. *Carbohydr Polym* 181:605–615. <https://doi.org/10.1016/j.carbpol.2017.11.106>
- Wang N, Ma W, Ren Z, Du Y, Xu P, Han X (2018) Prussian blue analogues derived porous nitrogen-doped carbon microspheres as high-performance metal-free peroxydisulfate activators for non-radical-dominated degradation of organic pollutants. *J Mater Chem A* 6(3):884–895. <https://doi.org/10.1039/C7TA08472B>
- Santoso E, Ediati R, Kusumawati Y, Bahruji H, Sulistiono DO, Prasetyoko D (2020) Review on recent advances of carbon based adsorbent for methylene blue removal from waste water. *Mater Today Chem* 16:100233. <https://doi.org/10.1016/j.mtchem.2019.100233>
- Lee J, Patel R (2022) Wastewater treatment by polymeric microspheres: a review. *Polymers (Basel)* 14:9. <https://doi.org/10.3390/polym14091890>
- Sun X et al (2014) Amino-functionalized magnetic cellulose nanocomposite as adsorbent for removal of Cr(VI): synthesis and adsorption studies. *Chem Eng J* 241:175–183. <https://doi.org/10.1016/j.cej.2013.12.051>

19. Shao Y, Zhou L, Bao C, Ma J, Liu M, Wang F (2016) Magnetic responsive metal–organic frameworks nanosphere with core–shell structure for highly efficient removal of methylene blue. *Chem Eng J* 283:1127–1136. <https://doi.org/10.1016/j.cej.2015.08.051>
20. Tai Y, Wang L, Gao J, Amer WA, Ding W, Yu H (2011) Synthesis of Fe<sub>3</sub>O<sub>4</sub>@poly(methylmethacrylate-co-divinylbenzene) magnetic porous microspheres and their application in the separation of phenol from aqueous solutions. *J Colloid Interface Sci* 360(2):731–738. <https://doi.org/10.1016/j.jcis.2011.04.096>
21. Wang C, Yan J, Cui X, Wang H (2011) Synthesis of raspberry-like monodisperse magnetic hollow hybrid nanospheres by coating polystyrene template with Fe<sub>3</sub>O<sub>4</sub>@SiO<sub>2</sub> particles. *J Colloid Interface Sci* 354(1):94–99. <https://doi.org/10.1016/j.jcis.2010.09.078>
22. Li Z, Wang Z, Wang C, Ding S, Li F, Lin H (2019) Preparation of magnetic resin microspheres M-P(MMA-DVB-GMA) and the adsorption property to heavy metal ions. *Appl Surf Sci* 496:143708. <https://doi.org/10.1016/j.apsusc.2019.143708>
23. Jiang J, Sun X, Li Y, Deng C, Duan G (2018) Facile synthesis of Fe<sub>3</sub>O<sub>4</sub>@PDA core-shell microspheres functionalized with various metal ions: a systematic comparison of commonly-used metal ions for IMAC enrichment. *Talanta* 178:600–607. <https://doi.org/10.1016/j.talanta.2017.09.071>
24. Xu Z, Xia A, Wang C, Yang W, Fu S (2007) Synthesis of raspberry-like magnetic polystyrene microspheres. *Mater Chem Phys* 103(2–3):494–499. <https://doi.org/10.1016/j.matchemphys.2007.02.074>
25. Gao J, Ran X, Shi C, Cheng H, Cheng T, Su Y (2013) One-step solvothermal synthesis of highly water-soluble, negatively charged superparamagnetic Fe<sub>3</sub>O<sub>4</sub> colloidal nanocrystal clusters. *Nanoscale* 5(15):7026–7033. <https://doi.org/10.1039/C3NR00931A>
26. Sun X, Yang L, Li Q, Liu Z, Dong T, Liu H (2015) Polyethyleneimine-functionalized poly(vinyl alcohol) magnetic microspheres as a novel adsorbent for rapid removal of Cr(VI) from aqueous solution. *Chem Eng J* 262:101–108. <https://doi.org/10.1016/j.cej.2014.09.045>
27. Zhang B, Zhang H, Fan X, Li X, Yin D, Zhang Q (2013) Preparation of thermoresponsive Fe<sub>3</sub>O<sub>4</sub>/P(acrylic acid-methyl methacrylate-*N*-isopropylacrylamide) magnetic composite microspheres with controlled shell thickness and its releasing property for phenolphthalein. *J Colloid Interface Sci* 398:51–58. <https://doi.org/10.1016/j.jcis.2013.01.042>
28. Liu T et al (2019) Tailor-made core/shell/shell-like Fe<sub>3</sub>O<sub>4</sub>@SiO<sub>2</sub>@PPy composites with prominent microwave absorption performance. *J Alloys Compd* 779:831–843. <https://doi.org/10.1016/j.jallcom.2018.11.167>
29. Cvek M et al (2015) A facile controllable coating of carbonyl iron particles with poly(glycidyl methacrylate): a tool for adjusting MR response and stability properties. *J Mater Chem C* 3(18):4646–4656. <https://doi.org/10.1039/C5TC00319A>
30. Dresco PA, Zaitsev VS, Gambino RJ, Chu B (1999) Preparation and properties of magnetite and polymer magnetite nanoparticles. *Langmuir* 15(6):1945–1951. <https://doi.org/10.1021/la980971g>
31. Zhang Y, Liu R, Hu Y, Li G (2009) Microwave heating in preparation of magnetic molecularly imprinted polymer beads for trace triazines analysis in complicated samples. *Anal Chem* 81(3):967–976. <https://doi.org/10.1021/ac8018262>
32. Arora G et al (2021) Fabrication, functionalization and advanced applications of magnetic hollow materials in confined catalysis and environmental remediation. *Nanoscale* 13(25):10967–11003. <https://doi.org/10.1039/D1NR01010G>
33. Liu S et al (2016) Magnetically separable and recyclable Fe<sub>3</sub>O<sub>4</sub>-polydopamine hybrid hollow microsphere for highly efficient peroxidase mimetic catalysts. *J Colloid Interface Sci* 469:69–77. <https://doi.org/10.1016/j.jcis.2016.02.011>
34. Wang J, Zhang W, Qian Y, Deng B, Tian W (2016) pH, temperature, and magnetic triple-responsive polymer porous microspheres for tunable adsorption. *Macromol Mater Eng* 301(9):1132–1141. <https://doi.org/10.1002/mame.201600161>
35. Nie Y, Luo Y, Luo S, Cao X, Song G, Deng C (2022) Amphiphilic copolymers grafted on monodisperse magnetic microspheres as an efficient adsorbent for the extraction of safrole in the plasma. *J Chromatogr A* 1662:462733. <https://doi.org/10.1016/j.chroma.2021.462733>
36. Yu B, He L, Wang Y, Cong H (2017) Multifunctional PMMA@Fe<sub>3</sub>O<sub>4</sub>@DR magnetic materials for efficient adsorption of dyes. *Materials (Basel)* 10(11):1–12. <https://doi.org/10.3390/ma10111239>
37. Dong Y, Wang S, Choi HJ (2022) Poly(*N*-methylaniline)/magnetite microsphere and its electrical and magnetic dual responses. *Polymer (Guildf)* 240:124492. <https://doi.org/10.1016/j.polymer.2021.124492>
38. Cao X et al (2019) Fabrication of functionalized magnetic microspheres based on monodispersed polystyrene for quantitation of allyl-benzodioxoles coupled with gas chromatography and mass spectrometry. *J Chromatogr A* 1607:460402. <https://doi.org/10.1016/j.chroma.2019.460402>
39. de la Escosura-Muñiz A, Plichta Z, Horák D, Merkoçi A (2015) Alzheimer's disease biomarkers detection in human samples by efficient capturing through porous magnetic microspheres and labelling with electrocatalytic gold nanoparticles. *Biosens Bioelectron* 67:162–169. <https://doi.org/10.1016/j.bios.2014.07.086>
40. Yang X, Chen L, Han B, Yang X, Duan H (2010) Preparation of magnetite and tumor dual-targeting hollow polymer microspheres with pH-sensitivity for anticancer drug-carriers. *Polymer (Guildf)* 51(12):2533–2539. <https://doi.org/10.1016/j.polymer.2010.04.032>
41. Horák D, Hlídková H, Klyuchivska O, Grytsyna I, Stoika R (2017) PEGylation controls attachment and engulfment of monodisperse magnetic poly(2-hydroxyethyl methacrylate) microspheres by murine J774.2 macrophages. *Appl Surf Sci* 426:315–324. <https://doi.org/10.1016/j.apsusc.2017.07.148>
42. Salih T, Ahlford A, Nilsson M, Plichta Z, Horák D (2016) Streptavidin-modified monodispersed magnetic poly(2-hydroxyethyl methacrylate) microspheres as solid support in DNA-based molecular protocols. *Mater Sci Eng C* 61:362–367. <https://doi.org/10.1016/j.msec.2015.12.061>
43. Koubková J et al (2014) Magnetic poly(glycidyl methacrylate) microspheres for protein capture. *N Biotechnol* 31(5):482–491. <https://doi.org/10.1016/j.nbt.2014.06.004>
44. Horák D et al (2014) Monodisperse carboxyl-functionalized poly(ethylene glycol)-coated magnetic poly(glycidyl methacrylate) microspheres: application to the immunocapture of  $\beta$ -amyloid peptides. *Macromol Biosci* 14(11):1590–1599. <https://doi.org/10.1002/mabi.201400249>
45. Horak D et al (2013) Albumin-coated monodisperse magnetic poly(glycidyl methacrylate) microspheres with immobilized antibodies: application to the capture of epithelial cancer cells. *J Biomed Mater Res A* 101A(1):23–32. <https://doi.org/10.1002/jbm.a.34297>
46. Horák D et al (2012) New monodisperse magnetic polymer microspheres biofunctionalized for enzyme catalysis and bioaffinity separations. *Macromol Biosci* 12(5):647–655. <https://doi.org/10.1002/mabi.201100393>
47. Kuan WC, Horák D, Plichta Z, Lee WC (2014) Immunocapture of CD133-positive cells from human cancer cell lines by using monodisperse magnetic poly(glycidyl methacrylate) microspheres containing amino groups. *Mater Sci Eng C* 34(1):193–200. <https://doi.org/10.1016/j.msec.2013.09.009>
48. Horák D, Hlídková H, Trachtová Š, Šlouf M, Rittich B, Španová A (2015) Evaluation of poly(ethylene glycol)-coated monodispersed magnetic poly(2-hydroxyethyl methacrylate) and poly(glycidyl

- methacrylate) microspheres by PCR. *Eur Polym J* 68:687–696. <https://doi.org/10.1016/j.eurpolymj.2015.03.036>
49. Man H, Nie Y, Shao S, Wang Y, Wang Z, Jiang Y (2022) Fabrication of Fe<sub>3</sub>O<sub>4</sub>@poly(methyl methacrylate-co-glycidyl methacrylate) microspheres via miniemulsion polymerization using porous microspheres as templates for removal of cationic dyes. *New J Chem* 46(28):13442–13453. <https://doi.org/10.1039/D2NJ01440H>
50. Yang Z, Peng H, Wang W, Liu T (2010) Crystallization behavior of poly( $\epsilon$ -caprolactone)/layered double hydroxide nanocomposites. *J Appl Polym Sci* 116(5):2658–2667. <https://doi.org/10.1002/app>
51. Sun X et al (2013) Synthesis of polyethylenimine-functionalized poly(glycidyl methacrylate) magnetic microspheres and their excellent Cr(VI) ion removal properties. *Chem Eng J* 234(1):338–345. <https://doi.org/10.1016/j.cej.2013.08.082>
52. Liu W, Zhu X, Yang X, Li K, Yang Z (2018) Preparation of highly cross-linked hydrophilic porous microspheres poly(N, N'-methylenebisacrylamide) and poly(N, N'-methylenebisacrylamide-co-acrylic acid) with an application on the removal of cadmium. *Polym Adv Technol* 29(11):2724–2734. <https://doi.org/10.1002/pat.4371>
53. Jiaqi Z, Yimin D, Danyang L, Shengyun W, Liling Z, Yi Z (2019) Synthesis of carboxyl-functionalized magnetic nanoparticle for the removal of methylene blue. *Colloids Surfaces A Physicochem Eng Asp* 572(February):58–66. <https://doi.org/10.1016/j.colsurfa.2019.03.095>
54. Yao T, Guo S, Zeng C, Wang C, Zhang L (2015) Investigation on efficient adsorption of cationic dyes on porous magnetic polyacrylamide microspheres. *J Hazard Mater* 292:90–97. <https://doi.org/10.1016/j.jhazmat.2015.03.014>
55. Wang G et al (2019) Novel Fe<sub>3</sub>O<sub>4</sub>@lignosulfonate/phenolic core-shell microspheres for highly efficient removal of cationic dyes from aqueous solution. *Ind Crops Prod* 127(29):110–118. <https://doi.org/10.1016/j.indcrop.2018.10.056>
56. Li Y, Hu Y, Ye S, Wu Y, Yang C, Wang L (2016) Functional polyaniline-assisted decoration of polystyrene microspheres with noble metal nanoparticles and their enhanced catalytic properties. *New J Chem* 40(12):10398–10405. <https://doi.org/10.1039/C6NJ02200F>
57. Amiri A, Baghayeri M, Sedighi M (2018) Magnetic solid-phase extraction of polycyclic aromatic hydrocarbons using a graphene oxide/Fe<sub>3</sub>O<sub>4</sub>@polystyrene nanocomposite. *Microchim Acta* 185(8). <https://doi.org/10.1007/s00604-018-2928-x>
58. Lei Y, Zhang X, Meng X, Wang Z (2022) The preparation of core-shell Fe<sub>3</sub>O<sub>4</sub>@SiO<sub>2</sub> magnetic nanoparticles with different surface carboxyl densities and their application in the removal of methylene blue. *Inorg Chem Commun* 139:109381. <https://doi.org/10.1016/j.inoche.2022.109381>
59. Zhang X, Bai R (2003) Surface electric properties of polypyrrole in aqueous solutions. *Langmuir* 19(26):10703–10709. <https://doi.org/10.1021/la034893v>
60. Sharma P, Hussain N, Borah DJ, Das MR (2013) Kinetics and adsorption behavior of the methyl blue at the graphene oxide/reduced graphene oxide nanosheet-water interface: a comparative study. *J Chem Eng Data* 58(12):3477–3488. <https://doi.org/10.1021/je400743r>
61. Li J, Zhang Q, Feng J, Yan W (2013) Synthesis of PPy-modified TiO<sub>2</sub> composite in H<sub>2</sub>SO<sub>4</sub> solution and its novel adsorption characteristics for organic dyes. *Chem Eng J* 225:766–775. <https://doi.org/10.1016/j.cej.2013.03.011>

**Publisher's Note** Springer Nature remains neutral with regard to jurisdictional claims in published maps and institutional affiliations.

Springer Nature or its licensor (e.g. a society or other partner) holds exclusive rights to this article under a publishing agreement with the author(s) or other rightsholder(s); author self-archiving of the accepted manuscript version of this article is solely governed by the terms of such publishing agreement and applicable law.